

# Hydration solids

<https://doi.org/10.1038/s41586-023-06144-y>

Received: 5 October 2017

Accepted: 27 April 2023

Published online: 7 June 2023

 Check for updates

Steven G. Harrellson<sup>1,8</sup>, Michael S. DeLay<sup>2,8</sup>, Xi Chen<sup>2,6</sup>, Ahmet-Hamdi Cavusoglu<sup>3,7</sup>, Jonathan Dworkin<sup>4</sup>, Howard A. Stone<sup>5</sup> & Ozgur Sahin<sup>1,2,✉</sup>

Hygroscopic biological matter in plants, fungi and bacteria make up a large fraction of Earth's biomass<sup>1</sup>. Although metabolically inert, these water-responsive materials exchange water with the environment and actuate movement<sup>2–5</sup> and have inspired technological uses<sup>6,7</sup>. Despite the variety in chemical composition, hygroscopic biological materials across multiple kingdoms of life exhibit similar mechanical behaviours including changes in size and stiffness with relative humidity<sup>8–13</sup>. Here we report atomic force microscopy measurements on the hygroscopic spores<sup>14,15</sup> of a common soil bacterium and develop a theory that captures the observed equilibrium, non-equilibrium and water-responsive mechanical behaviours, finding that these are controlled by the hydration force<sup>16–18</sup>. Our theory based on the hydration force explains an extreme slowdown of water transport and successfully predicts a strong nonlinear elasticity and a transition in mechanical properties that differs from glassy and poroelastic behaviours. These results indicate that water not only endows biological matter with fluidity but also can—through the hydration force—control macroscopic properties and give rise to a ‘hydration solid’ with unusual properties. A large fraction of biological matter could belong to this distinct class of solid matter.

Spores are highly rigid cell types formed by bacteria in response to environmental stresses<sup>19</sup>. Spores contain nanometre-sized pores<sup>20</sup>, and respond to changes in humidity by changing size<sup>11,14</sup> (Fig. 1a) and generating force<sup>15</sup>. In this study, we probed the flow characteristics of water in spores of *Bacillus subtilis* to investigate the potential effects of confinement on the physical properties of water in a hygroscopic biological material. The puzzling implications of our findings led us to develop a simple theory and perform further experiments. The results reveal an unusual class of solid matter emerging from water.

## Slow water transport in spores

To probe the relationship between water transport kinetics and pore size, we assumed that the humidity-dependent expansion of spores is owing to the expansion of the nanometre-sized pores, and we varied the pore size by subjecting spores deposited on nanomechanical cantilever sensors<sup>21</sup> to different setpoint relative humidity (RH) values. We then slightly perturbed the spore-water equilibrium at each setpoint RH with weak photothermal pulses (Fig. 1b and Extended Data Fig. 1) and monitored the bending of the cantilevers owing to the forces generated by the spores<sup>15</sup> (Fig. 1c). Relaxation time constants showed a nearly tenfold change (Fig. 1d and Extended Data Fig. 2), suggesting a strong influence of pore size on transport kinetics.

To determine the scaling behaviour of kinetics with average pore size,  $x$ , we assumed the average pore size is linearly related to the RH-dependent change in spore height,  $\Delta h$ , in Fig. 1a (that is,  $x/x_{\max} \approx \Delta h/\Delta h_{\max}$ , where  $\Delta h_{\max}$  and  $x_{\max}$  are the maximum height change and maximum pore size, respectively). We estimated  $x_{\max} \approx 1.5$  nm using the known sieving

properties and mass density of spores (Methods), and  $\Delta h_{\max} \approx 74$  nm using atomic force microscopy (AFM) measurements. The resulting kinetic rate (inverse time constant,  $\tau^{-1}$ ) versus pore size plot shows a power-law relationship  $\tau^{-1} \approx x^m$  (Fig. 1e), with an exponent  $m \approx 1.9$  (95% confidence interval 1.7, 2.1).

Considering that permeability varies with pore diameter, the observed scaling behaviour is consistent with a fluid-filled porous elastic material<sup>22</sup>. However, quantitatively, the results would imply an extremely high viscosity of pore water, about five orders of magnitude higher than the viscosity of water at room temperature (Methods), which suggests that mechanisms other than viscous drag might be responsible for the slowdown of water transport. Notably, consistent with this view, we observed an activation energy for water transport, about 10 kcal mol<sup>-1</sup>, much larger than that of bulk water<sup>23</sup>, about 4 kcal mol<sup>-1</sup> (Fig. 1f and Methods).

Interpreting our findings within the conventional framework of a fluid-filled porous elastic solid has another unusual implication. The linear poroelastic theory relates mechanical strain to pore fluid pressure with a parameter that depends on the elastic modulus of the matrix<sup>24</sup>. Assuming that the pore fluid pressure is governed by the chemical potential of water that varies with the logarithm of RH, the approximately linear variation of spore size with RH (Fig. 1a) implies that the biomolecular matrix forming the pore network must have a strongly nonlinear mechanical behaviour, which is not common in materials<sup>25,26</sup>. Taken together, the marked slowdown of water transport, the accompanying high activation energy and the implication for a strong nonlinearity of the biomolecular matrix call for a mechanistic explanation.

<sup>1</sup>Department of Physics, Columbia University, New York, NY, USA. <sup>2</sup>Department of Biological Sciences, Columbia University, New York, NY, USA. <sup>3</sup>Department of Chemical Engineering, Columbia University, New York, NY, USA. <sup>4</sup>Department of Microbiology and Immunology, Columbia University, New York, NY, USA. <sup>5</sup>Department of Mechanical and Aerospace Engineering, Princeton University, Princeton, NJ, USA. <sup>6</sup>Present address: Advanced Science Research Center (ASRC) at the Graduate Center of the City University of New York, New York, NY, USA. <sup>7</sup>Present address: Merck Digital Sciences Studio (MDSS), Newark, NJ, USA. <sup>8</sup>These authors contributed equally: Steven G. Harrellson, Michael DeLay. <sup>✉</sup>e-mail: os2246@columbia.edu

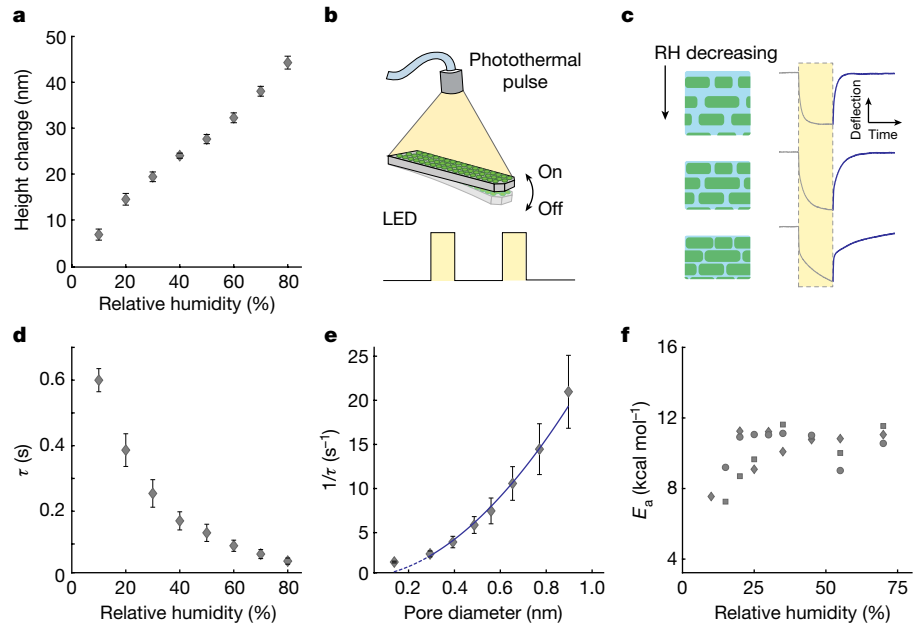


**Fig. 1 | Slow water transport in spores.** **a**, Change in spore height versus RH.

Data are mean  $\pm$  s.e.m. ( $n = 20$ ). **b**, Spores deposited on a cantilever are perturbed by weak photothermal pulses. **c**, Spores are subjected to different setpoint RH values to vary the pore sizes. The blue areas represent pore water and the green areas represent pore walls. The curves are examples of experimental data showing the cantilever deflection response to the photothermal stimulus (yellow region). The relaxation curves following the pulse (dark blue) are used to determine time constants. **d**, Time constants plotted against setpoint RH.

Data are mean  $\pm$  s.e.m. ( $n = 5$  measurements with separate cantilevers).

**e**, Inverse time constants (**d**) plotted against pore diameter. The solid blue line is the least-squares fit to data with a power-law relationship having an exponent equal to 1.9. The data point at 10% RH is excluded from the fit as the time constant is close to the pulse duration. Data are mean  $\pm$  s.e.m. ( $n = 5$  measurements with separate cantilevers). **f**, Activation energy ( $E_a$ ) versus RH. Data points are individual measurements. Repeated measurements done with three cantilevers are represented with marker shapes (circle, square and diamond).

## The hygroelastic model

Hydration forces are encountered when water is confined to nanometre-scale gaps<sup>16–18</sup> and could provide the physical basis for the unusual implications of our experiments. Hydration forces between hydrophilic surfaces are composed of an exponentially decaying smooth component and an oscillatory component (Fig. 2a). The oscillatory component stems from the tendency of water molecules to order near surfaces<sup>16</sup>, which can give rise to energy barriers against changes in confinement size and, more generally, against reconfiguration of confined water molecules that is reminiscent of jamming<sup>27,28</sup>. We therefore reasoned that migration of water molecules through expanding and contracting pores could be impeded by jamming-induced energy barriers<sup>29</sup>. In parallel, the smooth component could give rise to highly nonlinear equilibrium mechanical properties, not due to a nonlinear matrix, but due to exponentially decaying forces exerted by the pore fluid. We therefore hypothesized that hydration forces dominate pore mechanics for the hygroscopic spores.

In our hydration force-dominated model, the equilibrium pore size is governed by a balance between hydration forces and external factors, which are primarily the mechanical stress owing to external forces and the chemical potential of water set by the environment (Fig. 2b). Non-equilibrium responses to changes in mechanical stress or the chemical potential of water are governed by the oscillatory component of hydration forces, which impose jamming-driven kinetic limitations to the reconfiguration of water in pores and to changes in pore size (Fig. 2c). We refer to this two-stage description as the hygroelastic model.

The hygroelastic model predicts specific and highly unusual equilibrium and non-equilibrium mechanical properties that can be tested experimentally. In equilibrium, the model predicts a quantitative relationship between spore size and RH, and a quantitative relationship

between stress and strain that prescribes the value of elastic modulus and a strong nonlinear elasticity, all reflecting the rapid exponential decay of the smooth hydration force. The model also predicts a marked transition in elastic modulus at short timescales, when jammed water molecules are unable to rearrange and thereby acquire solid-like characteristics (Fig. 2d). We predict the transition to occur gradually over a range of timescales, as expected of thermally activated barrier crossing events (Fig. 2c). However, we note that this prediction differs from the compression-rate-dependent increase in the stiffness of confined fluids<sup>28</sup>, which is very small in magnitude and was thought to have requirements that are incompatible with the spores (Methods). Further, we expect the timescale of the predicted transition to be governed by diffusive dynamics, dependent on the length scale of perturbations as in poroelastic diffusion<sup>30</sup>.

## Dominant role of hydration forces

According to the hygroelastic model, forces owing to dehydration (decrease in chemical potential relative to fully saturated conditions) and compression (mechanical stress) are balanced by the exponentially decaying smooth hydration force. This balance can be expressed as

$$\sigma \approx Ae^{-x/\lambda} + \frac{k_B T}{\nu_w} \ln(\varrho). \quad (1)$$

Here,  $\sigma$  is the compressive stress due to external forces. The second term represents the hydration force, where  $A$  is the maximum pressure,  $x$  is the pore size and  $\lambda \approx 0.3$  nm is the decay length<sup>17,18</sup>, which is approximately equal to the size of a water molecule. The third term represents the chemical potential of water<sup>31</sup>, with  $k_B$ ,  $T$ ,  $\varrho$  and  $\nu_w$  being the Boltzmann constant, temperature, RH and the molecular volume of water, respectively. Other interaction forces are assumed to be small in

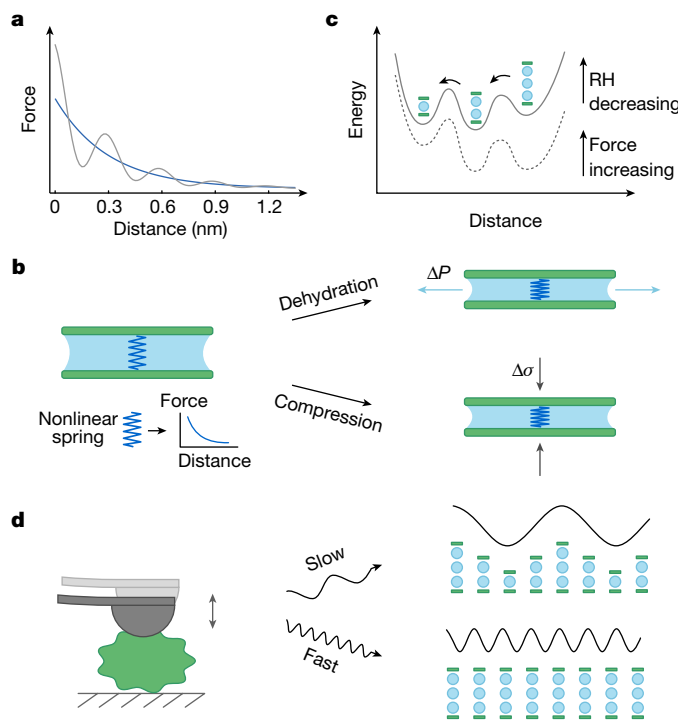


**Fig. 2 | The hygroelastic model.** **a**, Schematic of the hydration force (grey) and its exponentially decaying smooth component (blue). Distance values are given to indicate the short, subnanometre range of the hydration forces. **b**, Hydration forces between pore walls act as a nonlinear spring. This spring dominates all other mechanical restoration forces, including the stiffness of the biomolecular matrix forming the pores. Forces owing to dehydration (decrease in the chemical potential of water at low RH) act effectively as a decrease in pore fluid pressure ( $\Delta P$ ), acting on the nonlinear spring and compressing the pores, which is similar to the effect of mechanical stresses ( $\Delta\sigma$ ). **c**, Illustration of energy barriers against changes in pore size owing to changing RH or external forces. **d**, The hygroelastic model predicts that the pore water will exhibit solid-like characteristics when perturbed at short timescales (faster changes), illustrated here with an AFM tip applying an oscillating force.

magnitude and neglected; however, these ‘background forces’ would eventually be important near saturated conditions, when  $\varrho$  approaches 1.

We note that a balance between the hydration force and the chemical potential terms in equation (1) successfully predicts key features of water sorption isotherms in hygroscopic materials<sup>32</sup>. Here, equation (1) goes beyond the description of the equilibrium water content and asserts constitutive relationships that describe RH- and force-dependent deformations, as well as generation of force from changing RH.

As a simple test of equation (1), we plotted the magnitude of the third term,  $\frac{k_B T}{v_w} \ln(\varrho)$ , against  $x(\varrho)$ , the average pore size (previously determined for the analysis in Fig. 1e; Methods). According to equation (1), the resulting plot should be that of an exponential decay, with the decay length corresponding to  $\lambda$ . As predicted, the plot showed an exponentially decaying force (Fig. 3a), with a characteristic decay length  $\lambda = 0.32$  nm (95% confidence bounds 0.30–0.34 nm). This decay length is the hallmark of hydration forces, and therefore, this finding strongly supports the dominant role of hydration forces. Furthermore, the value of  $A$  in equation (1) is determined to be about 540 MPa, indicating the strength of hydration forces inside the pores.

### Water-responsive size change

Another striking consequence of equation (1) is that the water-responsive size change,  $\Delta h/h$ , depends primarily on the RH values of the starting and ending states,  $\varrho_0$  and  $\varrho$ , respectively, and structural parameters  $\lambda$  and  $l$ , the mean pore-to-pore distance, but not the chemical or mechanical properties of the biomolecular matrix:

$$\frac{\Delta h}{h} \approx \frac{\lambda}{l} \ln(\ln(\varrho_0)/\ln(\varrho)). \quad (2)$$

We estimated  $l$  from the geometric relationship  $x_{\max}/l \approx \Delta h_{\max}/h$ , for  $x_{\max} \approx 1.5$  nm,  $\Delta h_{\max} \approx 74$  nm and  $h \approx 308$  nm, the total thickness of the water-permeable layers of the spores (Methods). Shown in Fig. 3b, the experimental  $\Delta h$  values agree well with equation (2) under subsaturated conditions for  $l \approx 6.2$  nm. Because equation (2) diverges when  $\varrho$  approaches 1, we added a constant negative pressure term (−5 MPa, equivalent to the substitution  $\varrho \rightarrow 0.96\varrho$ ) to the right side of equation (1) to balance the hydration force and match the height change at  $\varrho = 1$ . These results show that the water-responsive size change of spores is governed by the hydration force.

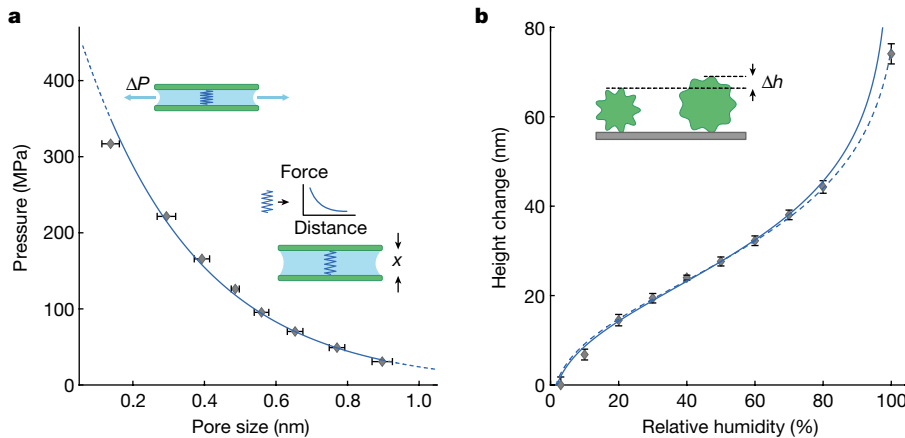


**Fig. 3 | Dominant role of hydration forces.** **a**, The magnitude of the effective pressure owing to chemical potential of water, calculated from RH, temperature and the molar volume of water, plotted against pore size (diamonds). Data are mean ± s.e.m. ( $n = 20$ ). The solid line is an exponential fit to the data. The dashed lines are extrapolations. Illustrations show the balance between the effective pressure,  $\Delta P$ , and the force due to a nonlinear spring, which determines the

pore size, denoted by  $x$ . **b**, Predicted spore height change with RH according to equation (2) (solid blue line) plotted with the mean height change against RH (diamonds). Data are mean ± s.e.m. ( $n = 20$  for RH from 10% to 80%, and  $n = 19$  for RH = 3% and RH = 100%). The dashed blue line corresponds to equation (2) after the substitution  $\varrho \rightarrow 0.96\varrho$  to account for background forces.

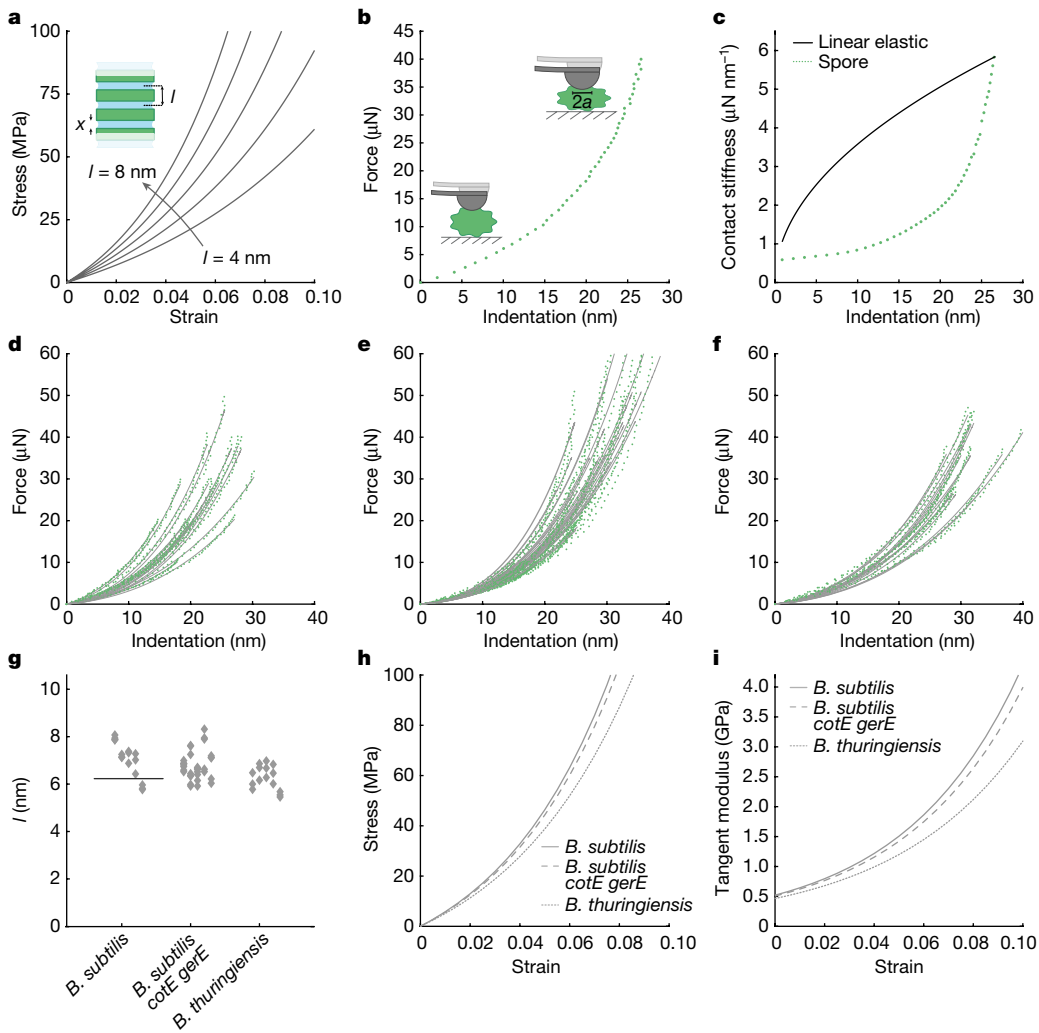


**Fig. 4 | Strong nonlinear elasticity.** **a**, Theoretical stress–strain curves for different values of  $l$ . **b**, A representative experimental force–indentation curve using a spherical AFM tip. The horizontal bar under the AFM tip illustrates the contact diameter ( $2a$ ). **c**, Contact stiffness versus indentation depth (green dotted line) and the theoretical contact stiffness of a linear elastic material with matching peak contact stiffness (solid black line). **d–f**, Force–indentation curves on multiple spores (green dotted lines) from *B. subtilis* (**d**), *B. subtilis* *cotE gerE* (**e**) and *B. thuringiensis* (**f**). The solid grey curves are least-squares fits

based on equation (5). **g**, Values of  $l$  determined in **d–f**. Data points from each individual spore are grouped vertically. The width of the 95% confidence intervals determined by the fit were less than 8% of the respective value of  $l$  for 59 of 63 curves, and between 15% and 21% for the remaining 4 curves. The horizontal line is  $l$  estimated independently using the change in spore height with RH. **h,i**, Stress–strain (**h**) and tangent modulus–strain (**i**) curves based on equations (3) and (4) using the mean values of  $l$  in **g**, plotted to highlight the degree of nonlinearity.

## Microscopic theory of elasticity

Equation (1) provides a microscopic theory of elasticity that relates elastic modulus to microscopic structure (mean pore-to-pore distance,  $l$ ), and the decay length of hydration forces,  $\lambda$ . By approximating strain,  $\epsilon$ , with the ratio of the change in pore size,  $\Delta x(\sigma)$ , to  $l$ ,  $\epsilon = \Delta x/l$ , and assuming incompressible pore walls, we can determine a stress–strain relationship:

$$\sigma(\epsilon) = \ln(1/\varrho) \frac{k_B T}{\nu_w} (e^{l\epsilon/\lambda} - 1). \quad (3)$$

This is a highly nonlinear relationship as  $l \gg \lambda$  (Fig. 4a). It is noted that  $l$  slightly varies with RH due to the changes in pore size. The corresponding tangent modulus,  $E_t = d\sigma/d\epsilon$  is given by:

$$E_t(\epsilon) \approx \ln(1/\varrho) \frac{k_B T}{\nu_w} \frac{l}{\lambda} e^{l\epsilon/\lambda}. \quad (4)$$

As a simple test of equation (4), we investigated the predicted strong nonlinearity by analysing force–indentation curves,  $F(z)$ , obtained by AFM<sup>15</sup> (Fig. 4b and Methods). We compared the scaling behaviour of the measured contact stiffness  $dF/dz$  with that of a linear elastic material. Although the latter scales with  $z^{1/2}$  for a spherical tip (Methods), the former is expected to be dominated by the exponentially growing  $E_t$  according to equation (4), because strain increases with indentation  $\epsilon(z)$ . The comparison in Fig. 4c shows the scaling behaviour of the experimental data is clearly different from that of a linear elastic material and grows increasingly faster with  $z$ , which support the response with strong nonlinear elasticity.

To test equation (4) quantitatively, we approximated the spore as a solid, cylindrical object (Extended Data Fig. 3), and derived an approximate force–indentation relationship based on this equation (Methods):

$$F(z) \approx 4 \ln(1/\varrho) \frac{k_B T R z}{\nu_w} e^{\frac{R l}{\lambda} \sqrt{\frac{z}{R}}}. \quad (5)$$

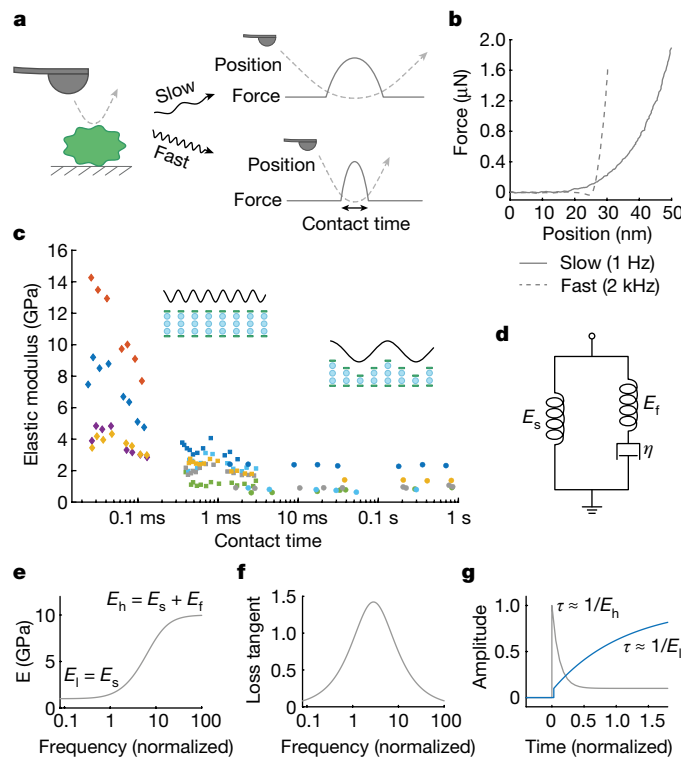


**Fig. 5 | The hygroelastic transition.** **a**, AFM force–distance curves are recorded at different modulation rates of vertical position. In the diagrams on the right, the dashed lines represent the time-dependent tip position and the solid lines represent the corresponding force. Contact time is indicated with a left-right arrow. **b**, Examples of force–distance curves recorded with slow (1 Hz) and fast (2 kHz) modulation rates. **c**, Elastic modulus estimated from force–distance curves plotted against the contact time. The colour represents individual spores and the marker shape represents the AFM method used: force ramp (round), and peak force tapping at 125 Hz (square) and at 2 kHz (diamond). **d**, Schematic of the standard linear solid model.  $E_s$  and  $E_h$  are elastic moduli and  $\eta$  is the viscosity. **e,f**, Frequency response (**e**) and the loss tangent (**f**) of the model in **d**. Frequency is normalized to  $E_s/\eta$ . **g**, Normalized step response of the model in **d** for a step change in displacement (grey) and a step change in force (blue). Time is normalized to  $\eta/E_s$ .  $E_l$  and  $E_h$  are defined in **e**, and they correspond to long-term and short-term elastic moduli.

Here  $\gamma$  is a numerical factor that accounts for non-uniform stress and strain throughout the sample and  $R$  is the effective radius of the indenter. Equation (5) successfully predicts the experimental force-indentation curves on multiple spore strains using only  $l$  as a parameter that is determined by curve fitting (Fig. 4d–f). The values of  $l$  were between 5 nm and 8 nm for *B. subtilis* strains, and between 5 nm and 7 nm for *Bacillus thuringiensis* (Fig. 4g). These numbers are very close to the value of  $l \approx 6.2$  nm, independently determined from the water-responsive height change (Fig. 3b).

The correspondence between independently determined values is remarkable because it means two seemingly distinct phenomena, water-responsive size change and force-induced deformation, are governed by a unified mechanism, consistent with the hydration-force-dominated behaviour. Furthermore, this analysis shows that equation (4) successfully predicts the elastic modulus of the spore and its nonlinearity, as highlighted in Fig. 4h,i.

### The hygroelastic transition

The hygroelastic model predicts an increase in elastic modulus at short timescales (Fig. 2d), which we refer as the hygroelastic transition. We investigated whether such a transition takes place by probing the elastic

modulus of spores using AFM<sup>33</sup> over a range of contact times (Fig. 5a and Methods).

Two examples of force–distance curves readily show a large increase in stiffness at short timescales (Fig. 5b). Measurements reveal a transition taking place from about 1 GPa to 10 GPa, and at a timescale of the order of about 0.1 ms (Fig. 5c). We also found that the relatively high values of elastic modulus at short timescales, about 10 GPa, is close to a rule of mixtures estimate for a solid composite (about 13 GPa; Methods).

To better understand the transition timescale, we considered a standard linear solid model (Fig. 5d–g and Methods). According to the model, the transition timescale is related to the diffusivity,  $D$ , estimated from the relaxation time constant measurements as follows:

$$t_{tr} \approx \frac{L^2 E_l}{D E_h}. \quad (6)$$

Here,  $L$  is the length scale of the diffusion, and  $E_h$  and  $E_l$  are the short- and long-term elastic moduli (Fig. 5g). Using  $D \approx 159 \text{ nm}^2 \text{ ms}^{-1}$  and  $L \approx 18 \text{ nm}$ , the contact radius (Methods), we find  $t_{tr} \approx 0.2 \text{ ms}$ , which is very close to the experimentally observed transition timescale (Fig. 5c).

These findings lend strong support for the hygroelastic model, which predicts that a jamming mechanism based on oscillatory hydration forces is responsible for both slow transport kinetics and the hygroelastic transition. Other mechanisms that could potentially explain the slow transport kinetics via an increase in pore fluid viscosity, for example, owing to polymers that might be dissolved in the pore fluid, would not necessarily cause a large transition in elastic modulus at short timescales. Rather, such systems would be expected to display poroelastic behaviour, albeit with slow kinetics.

### Discussion

Our findings show that hydration forces can dominate the mechanical properties of solids, captured by the hygroelastic model that relates macroscopic mechanical properties to microscopic interactions via the hydration force. As such, the hygroelastic model provides a microscopic theory for equilibrium, non-equilibrium and water-responsive mechanics. The ‘hygroelastic theory’ quantitatively explains the equilibrium properties including elastic modulus, size and nonlinearity, as well as how these properties respond to environmental conditions, and non-equilibrium properties including the nanoscale water transport characteristics, the kinetics of hydration and dehydration, and the transition in mechanical properties at short timescales. Importantly, the theory predicted some of these highly unusual behaviours that, to our knowledge, do not have counterparts in other types of materials. It is remarkable that an intermolecular force of single origin, the hydration force, can exert such a dominating influence and give rise to a rich set of solid and fluid mechanics phenomena in materials and so control corresponding material properties.

Although our experiments focused on bacterial spores, the simplicity and the minimal assumptions of the hygroelastic theory suggest that it could be applicable to other hygroscopic biological materials. Wood<sup>34</sup>, pollen grains<sup>12</sup>, fungal spores<sup>9</sup>, keratinous materials<sup>13</sup> and spider silk<sup>10</sup> all have elastic moduli of the same order as bacterial spores<sup>11,15</sup>, and their elastic modulus and size similarly vary with hydration. Notably, the hygroelastic theory offers a physical basis for the exponential-like decrease in elastic modulus of wood cell wall with hydration<sup>34</sup> and predicts its elastic modulus perpendicular to the cellulose crystals, of the order about 1 GPa, via equation (4) by setting  $\varrho = 0.5$  (50% RH) and  $l = 3 \text{ nm}$ , the approximate diameter of cellulose crystals<sup>35</sup>.

A consequence of the hygroelastic theory is a uniform mechanistic explanation of water-responsive size change with force-induced deformations (equation (1) and Fig. 4g), as mechanical stress is efficiently coupled into the chemical potential of pore water and vice versa. This feature could lead to efficient mechanical actuation, energy conversion

and storage systems, and harvesting of water from subsaturated environments. Furthermore, the strong nonlinear elasticity reported here could find uses in smart, adaptive materials and in mechanical computing<sup>36</sup>.

Another consequence of the hydroelastic theory is the prediction and subsequent discovery of the hydroelastic transition. The hydroelastic transition differs from both poroelastic and glassy behaviours that result in time-dependent mechanical behaviours in other materials. In poroelasticity, there is a short-time response that allows local rearrangements of solvent molecules and a long-time response that allows migration<sup>37</sup>. In the hydroelastic behaviour, the short-time response does not allow local rearrangements, leading to a substantial increase in elastic modulus at short timescales. The glass transition in polymers also exhibits pronounced timescale-dependent mechanics. But unlike glassy behaviour, the hydroelastic transition timescale is coupled to the length scale of mechanical perturbations owing to diffusive dynamics of the transition. Furthermore, macroscopically, the hydroelastic transition occurs between two elastic solid states, as opposed to a transition between glassy and liquid states. The hydroelastic transition, with its tunable frequency response, elasticity and damping characteristics, offers additional avenues for the development of smart, adaptive materials.

Our hydroelastic theory emphasizes that solid materials acquire their structural rigidity, the defining characteristic of the solid state, from the fluid permeating their pores; and that the macroscopic mechanical properties of the solid are governed by the fluid's microscopic properties via the hydration forces. Such 'hydration solids', which can exchange their essential constituent water with the environment and have it flow through the material, are potentially abundant in the environment.

## Online content

Any methods, additional references, Nature Portfolio reporting summaries, source data, extended data, supplementary information, acknowledgements, peer review information; details of author contributions and competing interests; and statements of data and code availability are available at <https://doi.org/10.1038/s41586-023-06144-y>.

1. Bar-On, Y. M., Phillips, R. & Milo, R. The biomass distribution on Earth. *Proc. Natl Acad. Sci. USA* **115**, 6506–6511 (2018).
2. Dawson, C., Vincent, J. F. V. & Rocca, A.-M. How pine cones open. *Nature* **390**, 668–668 (1997).
3. Elbaum, R., Zaltzman, L., Burgert, I. & Fratzl, P. The role of wheat awns in the seed dispersal unit. *Science* **316**, 884–886 (2007).
4. Fratzl, P. & Barth, F. G. Biomaterial systems for mechanosensing and actuation. *Nature* **462**, 442–448 (2009).
5. Dumais, J. & Forterre, Y. "Vegetable dynamicks": the role of water in plant movements. *Ann. Rev. Fluid Mech.* **44**, 453–478 (2012).
6. Burgert, I. & Fratzl, P. Actuation systems in plants as prototypes for bioinspired devices. *Phil. Trans. R. Soc. A* **367**, 1541–1557 (2009).
7. Chen, X. et al. Scaling up nanoscale water-driven energy conversion into evaporation-driven engines and generators. *Nat. Commun.* **6**, 7346 (2015).
8. Pasanen, A. L., Pasanen, P., Jantunen, M. J. & Kallikoski, P. Significance of air humidity and air velocity for fungal spore release into the air. *Atmos. Environ. Part A* **25**, 459–462 (1991).
9. Zhao, L., Schaefer, D. & Marten, M. R. Assessment of elasticity and topography of *Aspergillus nidulans* spores via atomic force microscopy. *Appl. Environ. Microbiol.* **71**, 955–960 (2005).
10. Agnarsson, I., Dhinojwala, A., Sahni, V. & Blackledge, T. A. Spider silk as a novel high performance biomimetic muscle driven by humidity. *J. Exp. Biol.* **212**, 1990–1994 (2009).
11. Sahin, O., Yong, E. H., Driks, A. & Mahadevan, L. Physical basis for the adaptive flexibility of *Bacillus* spore coats. *J. R. Soc. Interface* **9**, 3156–3160 (2012).
12. Qu, Z. & Meredith, J. C. The atypically high modulus of pollen exine. *J. R. Soc. Interface* **15**, 20180533 (2018).
13. Lazarus, B. S. et al. Engineering with keratin: a functional material and a source of bioinspiration. *iScience* **24**, 102798 (2021).
14. Westphal, A. J., Price, P. B., Leighton, T. J. & Wheeler, K. E. Kinetics of size changes of individual *Bacillus thuringiensis* spores in response to changes in relative humidity. *Proc. Natl Acad. Sci. USA* **100**, 3461 (2003).
15. Chen, X., Mahadevan, L., Driks, A. & Sahin, O. *Bacillus* spores as building blocks for stimuli-responsive materials and nanogenerators. *Nat. Nanotechnol.* **9**, 137–141 (2014).
16. Israelachvili, J. N. & Pashley, R. M. Molecular layering of water at surfaces and origin of repulsive hydration forces. *Nature* **306**, 249–250 (1983).
17. Rau, D. C. & Parsegian, V. A. Direct measurement of forces between linear polysaccharides xanthan and schizophyllan. *Science* **249**, 1278–1281 (1990).
18. Parsegian, V. A. & Zemb, T. Hydration forces: observations, explanations, expectations, questions. *Curr. Opin. Colloid Interface Sci.* **16**, 618–624 (2011).
19. Nicholson, W. L., Munakata, N., Horneck, G., Melosh, H. J. & Setlow, P. Resistance of *Bacillus* endospores to extreme terrestrial and extraterrestrial environments. *Microbiol. Mol. Biol. Rev.* **64**, 548–572 (2000).
20. Gerhardt, P. & Black, S. H. Permeability of bacterial spores II. *J. Bacteriol.* **82**, 750–760 (1961).
21. Mertens, J. et al. Label-free detection of DNA hybridization based on hydration-induced tension in nucleic acid films. *Nat. Nanotechnol.* **3**, 301–307 (2008).
22. Moendarbary, E. et al. The cytoplasm of living cells behaves as a poroelastic material. *Nat. Mater.* **12**, 253–261 (2013).
23. Krynicki, K., Green, C. D. & Sawyer, D. W. Pressure and temperature dependence of self-diffusion in water. *Faraday Discuss. Chem. Soc.* **66**, 199–208 (1978).
24. Biot, M. A. General theory of three-dimensional consolidation. *J. Appl. Phys.* **12**, 155–164 (1941).
25. Storm, C., Pastore, J. J., MacKintosh, F. C., Lubensky, T. C. & Janmey, P. A. Nonlinear elasticity in biological gels. *Nature* **435**, 191–194 (2005).
26. Sheiko, S. S. & Dobrynin, A. V. Architectural code for rubber elasticity: from supersoft to superfirm materials. *Macromolecules* **52**, 7531–7546 (2019).
27. Granick, S., Bae, S. C., Kumar, S. & Yu, C. Confined liquid controversies near closure? *Physics* **3**, 73 (2010).
28. Khan, S. H., Matei, G., Patil, S. & Hoffmann, P. M. Dynamic solidification in nanoconfined water films. *Phys. Rev. Lett.* **105**, 106101 (2010).
29. Liu, A. J. & Nagel, S. R. The jamming transition and the marginally jammed solid. *Annu. Rev. Condens. Matter Phys.* **1**, 347–369 (2010).
30. Hu, Y., Zhao, X., Vlassak, J. J. & Suo, Z. Using indentation to characterize the poroelasticity of gels. *Appl. Phys. Lett.* **96**, 121904 (2010).
31. Wheeler, T. D. & Stroock, A. D. The transpiration of water at negative pressures in a synthetic tree. *Nature* **455**, 208–212 (2008).
32. Bertinetti, L., Fratzl, P. & Zemb, T. Chemical, colloidal and mechanical contributions to the state of water in wood cell walls. *New J. Phys.* **18**, 083048 (2016).
33. Garcia, R. Nanomechanical mapping of soft materials with the atomic force microscope: methods, theory and applications. *Chem. Soc. Rev.* **49**, 5850–5884 (2020).
34. Kulasinski, K., Derome, D. & Carmeliet, J. Impact of hydration on the micromechanical properties of the polymer composite structure of wood investigated with atomistic simulations. *J. Mech. Phys. Solids* **103**, 221–235 (2017).
35. Fernandes, A. N. et al. Nanostructure of cellulose microfibrils in spruce wood. *Proc. Natl Acad. Sci. USA* **108**, E1195–E1203 (2011).
36. Yasuda, H. et al. Mechanical computing. *Nature* **598**, 39–48 (2021).
37. Hong, W., Zhao, X., Zhou, J. & Suo, Z. A theory of coupled diffusion and large deformation in polymeric gels. *J. Mech. Phys. Solids* **56**, 1779–1793 (2008).

**Publisher's note** Springer Nature remains neutral with regard to jurisdictional claims in published maps and institutional affiliations.

Springer Nature or its licensor (e.g. a society or other partner) holds exclusive rights to this article under a publishing agreement with the author(s) or other rightsholder(s); author self-archiving of the accepted manuscript version of this article is solely governed by the terms of such publishing agreement and applicable law.

© The Author(s), under exclusive licence to Springer Nature Limited 2023

## Methods

### Preparation of spore-coated cantilevers

WT spores (PY79) were prepared as previously described by exhaustion in sporulation medium<sup>38</sup>. HMX-10 AFM cantilevers (Bruker) were prepared by first masking the non-coated surface with a donor cantilever chip of equal height in a gel-pack cantilever holder. The cantilevers were pre-warmed atop a ceramic heater (Corning, PC-600D) and spores were deposited using a conventional gravity-feed dual action 0.3-mm painting airbrush (C2-30A) mounted at 10-cm distance using a minimal pressure (Extended Data Fig. 1).

### Measurement of relaxation kinetics

An environmental control unit (ECU) constructed of insulating polystyrene houses the spore-coated cantilevers (mounted in the head of a Bruker multimode atomic force microscope), sensors, temperature control elements and the light-emitting diode (LED) that supply photothermal pulses. Humidity inside the enclosure is measured using a Honeywell HIH-4021 and temperature with a thermocouple (Agilent U1180A) along with a data acquisition card (National Instruments NI-DAQ S-series 6115) coupled to a data acquisition program in LabVIEW. To achieve fine temperature control within the ECU, a series of thermoelectric coolers (Eathtek) is arrayed in parallel and connected to a variable power supply. A similar array of resistance-based heaters (WireKinetics) is connected to a separate power supply to adjust for the higher temperatures.

A stream of air is directed into the ECU opposite the atomic force microscope to vary the RH. Humidity is controlled by mixing dry air (about 5% RH) provided by a laboratory air source with humid air (>90% RH) generated by passing the laboratory air through a bubbler. An airstone (JW Pet Company) is used to bubble air into water in an Erlenmeyer flask. A variable power computer fan is positioned approximately 10 cm from the cantilever to facilitate evaporation and air mixture near the spores. A mild fan setting producing an air speed of 0.2 m s<sup>-1</sup> is used.

A variable power fibre-coupled 1,000-mA LED of wavelength 455 nm (M455F1, Thorlabs) is used to rapidly perturb the equilibrium of spores via photothermal heating. The LED is manipulated with a photography focusing-rail slider coupled to a stereotactic manipulator scavenged from a microscope stage such that the heat source may approach the cantilever within <1 mm. Finer manipulation and alignment of the LED to the cantilever is accomplished with endoscopes embedded within the ECU and positioned at the side and above the multimode atomic force microscope head. LED power is scaled manually such that the deflection during dry conditions is comparable in amplitude to that of the more humid conditions. The perturbation to equilibrium was kept small by using a low LED power and the magnitude of the perturbation was tested by comparing the shifts in cantilever resonance frequency between the on and off states of the LED with the shifts between different 10% and 80% RH (Extended Data Fig. 4).

A LabVIEW routine controls the timing of the triggering of the photothermal pulse, and collects cantilever deflection, humidity and temperature data. Data acquisition is timed via an external function generator and sampled with 5-ms resolution once temperature and humidity are stabilized within  $\pm 0.5\%$  (RH) and  $\pm 0.5^\circ\text{C}$ . A 3-s loop time is utilized to allow re-equilibration of the cantilever.

Bending signals show a gradual relaxation behaviour preceded by a rapid initial response, but we focused on the slower transients, as these dominate the overall responses except at very low setpoint RH. Relaxation time constants are determined offline by applying least-squares fit to the transients after the photothermal pulses and averaging over multiple cycles. Scaling behaviour of the relaxation time constants are obtained by least-squares fit to the natural logarithm of the inverse time constants with a linear relationship that includes the slope and an offset as fit parameters.

### Estimation of pore diameter

To relate response times to the dimensions of spore nanopores, we estimated pore dimensions as a function of RH. The permeability of spores to small molecules such as glucose and amino acids that have dimensions less than 1 nm across, and the sieving of larger biopolymers, characterized by the decreased uptake of polyethylene glycols by spores of *Bacillus cereus* larger than molecular weight of 4,000 (ref. 39), which has radius of gyration,  $R_g$ , around 2.4 nm (ref. 40) and its corresponding hydraulic radius ( $R_h \approx R_g/1.59$ )<sup>41</sup> around 1.5 nm, suggests that the nominal diameter of spore nanopores in the fully hydrated state is in the range of 1 nm to 2 nm. We therefore estimate the nominal pore dimensions in the fully hydrated state to be 1.5 nm. To estimate pore dimensions in the opposite extreme, that is, when spores are dried under vacuum, we relied on previous findings that the mass density of vacuum-dried spores is in the range of 1.45–1.50 g cm<sup>-3</sup> (ref. 42), which is about the same as the density of proteins determined based on their crystal structures<sup>43</sup> (1.35 g cm<sup>-3</sup> to 1.55 g cm<sup>-3</sup>). This comparison suggests that vacuum-dried spores must contain only a small amount of water. This interpretation is also consistent with the buoyant mass-density measurements<sup>44</sup> that estimate the density of the dry region of the spore (that is, the biomolecular matrix) to be 1.45 g cm<sup>-3</sup> by substituting water with D<sub>2</sub>O. Therefore, spore nanopores are likely to contract almost completely when RH approaches 0%. Thus, we estimate that the nominal pore diameter changes from 0 nm to 1.5 nm approximately linearly with the change in overall spore height as measured by AFM (Fig. 1a). We note that an immobile water layer could be considered as part of the pore walls and would not affect the quantitative results. Furthermore, uncertainties in the maximum pore size would proportionally affect the estimation of  $\lambda$ , but not  $\lambda/l$  because  $l$  is determined in relation to  $\lambda$ .

### Estimation of coat and cortex thicknesses

The total thickness,  $L$ , of the water-permeable coat and cortex layers are estimated from two modes of measurement using the calibrated scale bars and the ImageJ software package (NIH). First, we performed focused ion beam scanning electron microscopy on vacuum-dried wild-type spores and measured the depth of the cortex to be  $68.82 \pm 3.35$  nm ( $n = 10$  spores). We then made 90-nm microtomed sections of the spores and measured the cortex thickness by standard tapping mode AFM to be  $72.72 \pm 3.51$  nm ( $n = 25$ , 5 measurements each on 5 spores). These values agree with previous reports derived from measurements with the transmission electron microscope that also show the coat and the cortex have similar thicknesses<sup>45–47</sup>. We add the coat and cortex thickness values to approximate the thickness of fully dried spore's water-responsive material as 140 nm. This layer expands with RH. Using the increase in spore height at 50% RH (Fig. 1a), we determine the nominal thickness of water-permeable region at 50% RH to be 154 nm. The corresponding total thickness of the water-permeable region across the diameter of the spore is twice this amount, 308 nm.

### Estimation of diffusivity and viscosity within the poroelastic framework

We analysed the time constants in Fig. 1d according to poroelastic-like diffusive dynamics:

$$\tau \approx L^2/D, \quad (7)$$

where  $\tau$  is the relaxation time constant,  $L$  is the characteristic length scale of the diffusion and  $D$  is the diffusivity. Although spores deposited on cantilevers have multiple layers, two observations suggest that the characteristic length scale of the diffusion is set by the dimensions of individual spores. First, response times of individual spores probed by AFM are on the order of 100 ms, which is close to the time constants measured by the nanomechanical cantilever sensors. Second, the

quantity of spores we apply to cantilevers do not predictably alter the experimental time constant, rather, a change in spore structure via a mutation in *cotE gerE* that eliminates majority of spore coat proteins<sup>48</sup> (and reduces coat thickness) results in significantly faster response kinetics (Extended Data Fig. 5), which is consistent with the rate-limiting step being the diffusive dynamics in individual spores. The spore's outer layers, coat and the cortex are water permeable<sup>49</sup>; therefore, the total thickness of these layers determine  $L$ .

To estimate the diffusivity more precisely than the simple scaling relationship  $\tau \approx L^2/D$ , we considered the boundary conditions and used the solution for the one-dimensional diffusion problem with a constant concentration on one end and an insulating boundary at a distance  $L$ . (It is noted that the water-permeable layers rest on the spore core that exhibits little to no water exchange in the dormant state. Thus, the core sets an insulated boundary condition against diffusion.) This approach has been previously applied to poroelastic films<sup>50</sup>. It can be shown that the time constant  $\tau$ , defined as the time point when the average pressure reduces by a factor  $e$ , the base of natural logarithm, is given by

$$\tau = \alpha L^2/D, \quad (8)$$

where  $\alpha$  is approximately 0.32. At 50% RH, with an average time constant of 134 ms (Fig. 1d), we obtain  $D \approx 57 \text{ nm}^2 \text{ ms}^{-1}$ , and with an average time constant of 47.7 ms at 80% RH, we obtain  $D \approx 159 \text{ nm}^2 \text{ ms}^{-1}$ .

The observed kinetics of water transport in Fig. 1d imply an extremely high pore viscosity, if the results are interpreted within the framework of a fluid-filled porous elastic solid. To illustrate this point, we used a microscopic model of poroelasticity<sup>22</sup>, and estimated the magnitude of viscosity that would be needed to account for the slowdown if the change in the kinetic rate  $\tau^{-1}$  was entirely owing to an increase in viscosity. This model accounts for the hydraulic resistance of pores and relates diffusivity,  $D$ , to the elastic modulus,  $E$ , Poisson's ratio,  $\nu$ , pore diameter,  $x$ , viscosity of the pore fluid,  $\eta$ , porosity,  $\varphi$ , and the geometric features (for example, tortuosity) of the pore network represented by  $\kappa$ :

$$D = \frac{1}{16} \frac{(1-\nu)}{(1+\nu)(1-2\nu)} \frac{\varphi E x^2}{\kappa \eta}. \quad (9)$$

The value of  $D$  is independently determined from equation (8). To obtain an order of magnitude estimate of the viscosity, we used  $D \approx 57 \text{ nm}^2 \text{ ms}^{-1}$ ,  $\nu = 0.3$ ,  $\varphi = 0.15$ ,  $E = 6 \text{ GPa}$  (as determined by AFM<sup>15</sup>),  $\kappa = 4$  and  $x = 0.56 \text{ nm}$ , which resulted in  $\eta = 104 \text{ Pa s}$ , which is five orders of magnitude larger than the bulk viscosity of water at room temperature (about 1 mPa s). Because confinement of water does not necessarily lead to a substantial increase in viscosity<sup>51</sup>, the large value of  $\eta$  suggests additional mechanisms might slow down water transport in spores.

### Estimation of activation energy

The activation energy associated with the relaxation kinetics measurements is determined using an Arrhenius-type exponential relationship  $\tau \approx e^{E_a/RT}$ , where  $E_a$  is the activation energy,  $R$  is the molar gas constant and  $T$  is temperature. Accordingly,  $E_a$  can be estimated from the changes in relaxation rate of spores with temperature. However, owing to the temperature dependence of the chemical potential,  $\mu = k_B T \ln Q$ , varying temperature at constant RH will affect equilibrium pore size and thereby the relaxation kinetics. Therefore, this coupling must be taken into account before determining the activation energy. By separating the pore size dependence of kinetics,  $H(\mu)$ , from the exponential factor, we can express the relaxation rate,  $S$  (inverse time constant), as follows:

$$S(\mu, T) = H(\mu) e^{-E_a/k_B T}. \quad (10)$$

Using an empirical relationship for  $H(Q) \approx H_0 Q^m$ , which approximates the data in Fig. 1d for  $m = 1.2$  (determined by the slope of the linear least-squares fit to the natural logarithm of the time constants as a

function of  $\ln(Q)$ ), and defining an apparent activation energy,  $E_{app}$ , as the slope of the  $\ln(1/T)$  versus  $1/k_B T$  curve, one can show that the activation energy is related to  $E_{app}$  by

$$E_a = E_{app} - m k_B T \ln(Q). \quad (11)$$

The value of  $E_a$  is determined from the temperature-dependent measurements of relaxation time constants according to equation (11).

### Relationship to rate-dependent changes in confined fluids

The possibility of molecular jamming in confined water films was previously considered in experiments with an atomic force microscope<sup>28</sup>. When the confined fluid is compressed at increasing rates, the stiffness and damping characteristics of the confined fluid change in a rate-dependent manner. However, the change in stiffness observed in the experiments<sup>28</sup> is too small to have a substantial impact on the elastic modulus of a material with gigapascal-scale elastic modulus. To illustrate this point, we determine an effective elastic modulus value for the confined fluid,  $E_f = kd/S$ , using the measured stiffness,  $k$  ( $1 \text{ N m}^{-1}$  to  $10 \text{ N m}^{-1}$ ), the effective thickness of the confined fluid,  $d$  (about 1 nm, about three to four layers of water) and the effective area,  $S \approx 2\pi R d$ , where  $R \approx 100 \text{ nm}$  is the tip radius. With  $E_f \approx k/2\pi R$  we estimate the effective elastic modulus of the confined fluid to be around 1.6 MPa to 16 MPa, depending on the rate of compression. Therefore, a substantial change in the elastic modulus of a material with gigapascal-scale elastic modulus would not be expected. In contrast, the hydroelastic model predicts that the jammed state should exhibit a very high elastic modulus, comparable to that of ice.

Further, atomically smooth confining surfaces were thought to be necessary for the rate-dependent effects<sup>28</sup>. The hydroelastic model predicts that jamming-driven transition should occur even when water is confined between the rough surfaces of the spore interior. We reasoned that although parallel smooth surfaces make it possible to observe oscillatory hydration forces in the experiments, the underlying forces that govern the organization of water in confined spaces should still impose energy barriers against reorganization of water molecules, regardless of the morphology of the confining surfaces.

Another distinction of the hydroelastic model from previous interpretations of rate-dependent mechanical changes in the confined fluid is about the timescale of the changes. Previously, the critical timescale for stiffness increase was thought to be an intrinsic property of the confined fluid and its thickness<sup>52</sup>. Here we reasoned that the timescale should be governed by the kinetics of water transport in the confined space. In the context of a porous elastic material, the kinetics can be expected to be a diffusion-like process, as in poroelastic diffusion.

### Measurement of spore height

Topographic imaging of spores in different RH levels is performed in tapping mode using a multimode atomic force microscope (Bruker) housed within a separate scanner-mounted ECU. Humidity is adjusted as described for the ECU used in relaxation kinetic measurements with an identical sensor mounted <1 cm from the sample. Glass beads (750 nm, Corpuclar) are mixed 1:1 with the spore suspension for absolute size-change reference and to account for any piezo-induced artefacts of the high humidity. The sample is dispersed onto a mica substrate (Ted Pella) for imaging. Germinated, or otherwise unresponsive, spore shells are excluded from analysis. The image is processed for plane fit and maximal cross-sectional height relative to the substrate is obtained using the Nanoscope software package (Bruker). Heights of different spores are normalized using the average height of all spores. A separate set of measurements is performed to determine the maximum height change of spores. For these measurements, spore height is measured under 3% RH, 50% RH and when spores are immersed in water. The measurement at 50% RH is used to calibrate these measurements against the first set of measurements; therefore,

# Article

the height measurement at 50% is not used in the analysis of height versus RH in Fig. 3b.

## Analysis of force-indentation curves

Force-indentation curves were obtained previously using a force-RH cycle experiment<sup>15</sup>. Measurements were done at 90% RH and the forces recorded as the tip retracts from the surface are used to produce force-indentation curves with indentation depth in the range of 15 nm to 40 nm. Each curve was recorded over a duration of 1 s. Experiments were done on five spores of each *B. subtilis*, *B. subtilis cotE gerE* and *B. thuringiensis* with increasing depths of indentation. The dataset includes one force curve on each spore that was reported in ref. 15.

To analyse the force-indentation curves, we derived an approximate analytical expression for the force-indentation curves by considering the nonlinear stress-strain relationship, which is represented by tangent modulus  $E_t(\epsilon)$ . Although some biological structures are better modelled as stiff shells<sup>53</sup>, based on the known aspects of spore microstructure (Extended Data Fig. 3), we approximated the spore as a solid, cylindrical object that is indented by a spherical tip. Although the spore is composed of layers, for simplicity, we treated the spore as a homogeneous material. It is noted that similarities between the force-indentation curves measured on the wild type (Fig. 4d) and the *cotE gerE* strain that has its coat layer largely eliminated (Fig. 4e) indicate that the mechanical properties of the coat and the cortex layers are not substantially different. As the stress field in the substrate is non-uniform, we used an effective strain defined by  $\epsilon^* = yz/a$ , with  $a$  being the contact radius and  $y$  being a proportionality factor. For a spherical indenter the contact radius is related to the effective radius of the indenter,  $R$ , and the indentation depth,  $z$ , by  $a = \sqrt{Rz}$  (ref. 54). The contact stiffness is given by  $dF/dz = 2E_t(\epsilon^*)a$ . After substituting,  $E_t$ ,  $\epsilon^*$  and  $a$ , the function  $F(z)$  can be obtained by the following integral:

$$F(z) = 2\ln(1/\varrho) \frac{k_B T}{v_w} \frac{l}{\lambda} \int_0^z \sqrt{Rz'} e^{y\frac{l}{\lambda}\sqrt{\frac{z'}{R}}} dz'. \quad (12)$$

The result of the integral in equation (12) is the following:

$$F(z) \approx 4\ln(1/\varrho) \frac{k_B T R^2}{v_w \gamma^3} \left[ \left( \gamma^2 \frac{z}{R} - 2\gamma \frac{\lambda}{l} \sqrt{\frac{z}{R}} + 2 \frac{\lambda^2}{l^2} \right) e^{y\frac{l}{\lambda}\sqrt{\frac{z}{R}}} - 2 \frac{\lambda^2}{l^2} \right]. \quad (13)$$

A further simplification can be arrived at by noting that  $\lambda \ll l$ , which results in equation (5). To estimate the value of  $y$ , we considered the spatial variation of stress for a spherical indenter. In the case of a linear elastic material, the stress distribution in the sample is expressed analytically<sup>54</sup>, and it can be shown that 50% of the sample deformation takes place in the top layer of the sample having a thickness of  $0.9a$ . Therefore, we approximated  $y \approx 0.5/0.9$ , which is about 0.55. Although a nonlinear stress-strain relationship could affect the spatial variation of stress, the value of  $y$  derived from the linear case provides a simple approximation.

We used equation (5) to fit the data using  $l$  as a fit parameter. When calculating the effective radius of the indenter,  $R$ , we took into account the approximately cylindrical shape of the spores<sup>55</sup>, which resulted in 484 nm, 474 nm and 520 nm for *B. subtilis*, *B. subtilis cotE gerE* and *B. thuringiensis*, respectively. As these experiments were done at 90% RH, we substituted  $\varrho \rightarrow 0.96\varrho$  to account for background forces. To account for uncertainty in contact points, we substituted  $z \rightarrow z + z_0$  and used  $z_0$  as a fit parameter and restricted  $z_0$  to the range of 0–5 nm. Curve fitting was performed with MATLAB (MathWorks) using the ‘Non-linearLeastSquares’ method along with the ‘Trust-Region’ algorithm.

We note that other sources of nonlinearity can be present, but we neglect them because the observed nonlinearity is strong. We considered geometric nonlinearities owing to a layer being attached to a rigid substrate. For infinitely rigid substrates, a condition in which the

geometric nonlinearity would be the strongest, analytical expressions that account for geometric nonlinearities are available<sup>56</sup>. The expression for a paraboloid indenter, which approximates the spherical tip, is as follows:

$$F_{\text{sphere}} = F_0 \left[ 1 + \frac{1.133\sqrt{zR}}{h} + \frac{1.497zR}{h^2} + \frac{1.469(zR)^{\frac{3}{2}}}{h^3} + \frac{0.755(zR)^2}{h^4} \right]. \quad (14)$$

Here  $F_0$  is the force corresponding to the linear elastic case,  $z$  is the indentation depth,  $R$  is the tip radius and  $h$  is the layer thickness. Because contact stiffness,  $dF_{\text{sphere}}/dz$ , depends linearly on elastic modulus, we determined the ratio of contact stiffnesses for the case of a finite layer thickness and an infinite layer thickness to obtain the degree of geometric nonlinearity. For  $h = 700$  nm, the approximate diameter of a spore,  $z = 40$  nm, and an effective tip radius of  $R \approx 480$  nm, we find that geometric effects could lead to 43% increase in effective elastic modulus. The experimental results, fitted by equation (4), show approximately 20-fold increase in elastic modulus at 40-nm indentation. Although the spore is not a thin layer, this comparison is nonetheless useful to show that the nonlinearity observed in the experiment is much larger than geometric nonlinearities owing to the presence of a rigid substrate. Potential geometric nonlinearities due to the thinner outer layers of the spores (170 nm) or the spore radius (350 nm) can similarly be neglected because spore layers are expected to have comparable elastic moduli. Indeed, experiments do not show an increase in nonlinearity when spores that have their coats largely removed are probed (*Bacillus subtilis cotE gerE*; Fig. 4e,g).

We also considered the viscoelastic behaviour of spore layers. Viscoelastic response could result in force-indentation curves that exhibit nonlinearity. However, viscoelastic behaviour in spores would have a substantial effect on our other experiments. Force-indentation curves in Fig. 4 are recorded on a timescale of about 1 s and at 90% RH. Neither the relaxation time constant measurements in Fig. 1 nor the timescale-dependent stiffness measurements in Fig. 5 indicate a viscoelastic response at 1-s timescale.

## Dynamic nanomechanical measurements

*B. subtilis cotE gerE* spores are plated on mica (Electron Microscopy Sciences) and indented using silicon cantilevers with tip radii of approximately 750 nm and stiffness of approximately 250 N m<sup>-1</sup> (Team Nanotech). Spores are located using a confocal microscope (Zeiss LSM 800) in tandem with a Bioscope Resolve atomic force microscope in peak force tapping (PFT) mode (Bruker). Once located, the AFM probe is centred directly above the spore. The humidity is monitored and controlled as described previously in the measurement of spore height and is maintained at a level between 73% and 80% RH for dynamic nanomechanical measurements.

We combined two different AFM modes that collectively span contact times varying 5 orders of magnitude, from about 10 μs to about 0.4 s. We used a large tip to increase the tip-sample contact radius that sets the length scale of the mechanical perturbations. The ramp mode is used for low-frequency indentation and the PFT mode is used for high frequency. The ramp mode allows for a continuous variation in applied frequency, whereas the PFT mode is performed only at 125 Hz and 2,000 Hz. In ramp mode experiments, the ramp frequency is changed to modulate the probe-sample contact time. In PFT experiments, the frequency of the probe oscillation is fixed; contact time is modulated by maintaining a constant peak force value and changing the ramp height. Contact time is measured offline from the recorded force-time waveforms.

In the PFT mode, the calibration of the driving piezo is dependent on the ramp size and frequency. The true piezo sensitivity is determined by measuring the deflection sensitivity of a pre-calibrated probe. Shifts in the apparent deflection sensitivity are caused by amplitude- and

frequency-dependent changes in piezo calibration and are corrected by scaling the final force-indentation curves.

Force curve data are collected using the Nanoscope software package (Bruker) and processed using the MATLAB (Mathworks) Nanoscope analysis toolbox obtained from Bruker Nano Surfaces Division. Individual force curves are analysed in MATLAB and filtering of measurement noise and corrections for piezo sensitivity are made. The effective elastic modulus is computed by fitting force-indentation curves with the Derjaguin–Muller–Toporov model<sup>54</sup>. We used an effective radius of indenter  $R = 276.4\text{ nm}$ . To minimize the effects of nonlinear elasticity, peak force values were kept approximately around  $F_p = 1.5\text{ }\mu\text{N}$ . We estimated the nominal contact radius at the transition to be half of the peak contact radius during the force ramp. The peak contact diameter can be determined using the Hertz formula  $F = (4/3)Ea^3/R$ . Assuming that the transition occurs when the elastic storage modulus,  $E$ , is the arithmetic mean of  $E_h$  and  $E_l$ , about 6 GPa, and using  $R = 276.4\text{ nm}$  and  $F_p = 1.5\text{ }\mu\text{N}$ , one can find  $a \approx 36\text{ nm}$ , and thereby  $L \approx 18\text{ nm}$ .

### Rule of mixtures analysis

The short-timescale elastic modulus of the spore is estimated via rule of mixtures. To apply rule of mixtures, we considered the short-timescale mechanical characteristics of the spore to be that of a composite with two components: the predicted jammed state of pore fluid and the biomolecules that form the pore walls. We estimated the volume ratios of the two components using the average pore size,  $x \approx 0.9\text{ nm}$  (at 80% RH), and the mean pore-to-pore distance,  $l \approx 6.2\text{ nm}$ . For simplicity, we assumed pore walls have square cross-sections with edge lengths of  $l - x$ . This assumption leads to volume fractions of 0.3 and 0.7 for the pore fluid and the pore wall. We estimated the elastic modulus of the pore walls from the elastic modulus of the spore at low RH (about 7%) when pore volume gets negligibly small, which was measured via AFM force curves to be approximately 15 GPa. We estimated the elastic modulus of the predicted jammed phase of water with the elastic modulus of polycrystalline ice<sup>57</sup>, which is approximately 9.5 GPa. It is noted that the predicted jammed state of water in short timescales is not ice; however, in the absence of a direct measurement of the properties of this state, the elastic modulus of polycrystalline ice serves as a crude approximation. In addition, the high bulk modulus of water, approximately 2 GPa, points to a low compressibility, which the jammed state of water would be expected to inherit. Using the estimated values of the volume fractions and elastic modulus values of the two components, we applied the rule of mixtures as  $1/E_c = f_1/E_1 + f_2/E_2$ , where  $E_c \approx 13\text{ GPa}$  is the elastic modulus of the composite, and  $f_1, f_2, E_1$  and  $E_2$  are the volume fractions of the pore fluid and the pore walls. It is noted that the inverse relationship is consistent with the linear model used to estimate the equilibrium elastic modulus via equation (4).

### The standard linear solid model

By considering the elements of the standard linear solid model (Fig. 5d) in series and parallel, the time evolution of stress  $\sigma$  and strain  $\epsilon$  can be described in the form of a differential equation in terms of  $E_s, E_f$  and  $\eta$ :

$$\frac{d\sigma}{dt} + \frac{E_f}{\eta}\sigma = (E_s + E_f)\frac{d\epsilon}{dt} + \frac{E_s E_f}{\eta}\epsilon. \quad (15)$$

The frequency response  $F_\sigma(\omega)$  of stress is given by:

$$F_\sigma(\omega) = \frac{j\omega(E_s + E_f) + \frac{E_s E_f}{\eta}}{j\omega + \frac{E_f}{\eta}}. \quad (16)$$

Here  $j$  is the imaginary unit. The frequency response of strain  $F_\epsilon(\omega)$  is the inverse of the frequency response of stress:  $F_\epsilon(\omega) = 1/F_\sigma(\omega)$ . The step responses can be obtained from the respective frequency responses of stress and strain, or from equation (15).

The standard linear solid model shows that although damping is low away from the transition, the loss tangent reaches approximately 1.5 near the transition for  $E_h/E_l = 10$ , which is extremely high for a rigid elastic material. Importantly, according to the model, force relaxation occurs faster than displacement relaxation by a factor of  $E_h/E_l$  (Fig. 5g).

### Data availability

Source data for Figs. 1a,d–f, 3a,b, 4a–i and 5b,c, and Extend Data Figs. 2, 4 and 5 are included with the paper. The raw data for cantilever deflections (Fig. 1c–f), spore height (Figs. 1a and 3a,b), force–distance curves (Fig. 4b–f) and dynamic stiffness measurements (Fig. 5c) are available in figshare (<https://doi.org/10.6084/m9.figshare.22189823>)<sup>58</sup>.

### Code availability

The MATLAB codes used for data processing, curve fitting, and plotting are available in figshare (<https://doi.org/10.6084/m9.figshare.22189823>)<sup>58</sup>.

38. Harwood, C. R. & Cutting, S. M. *Molecular Biological Methods For Bacillus* (Wiley, 1990).
39. Scherrer, R., Beaman, T. C. & Gerhardt, P. Macromolecular sieving by the dormant spore of *Bacillus cereus*. *J. Bacteriol.* **108**, 868–873 (1971).
40. Rubinson, K. A. & Krueger, S. Poly(ethylene glycols) 2000–8000 in water may be planar: a small-angle neutron scattering (SANS) structure study. *Polymer* **50**, 4852–4858 (2009).
41. Dünweg, B., Reith, D., Steinhauser, M. & Kremer, K. Corrections to scaling in the hydrodynamic properties of dilute polymer solutions. *J. Chem. Phys.* **117**, 914–924 (2002).
42. Carrera, M., Zandomeni, R. O. & Sagripanti, J.-L. Wet and dry density of *Bacillus anthracis* and other *Bacillus* species. *J. Appl. Microbiol.* **105**, 68–77 (2008).
43. Fischer, H., Polikarpov, I. & Craievich, A. F. Average protein density is a molecular-weight-dependent function. *Protein Sci.* **13**, 2825–2828 (2004).
44. Knudsen, S. M. et al. Water and small-molecule permeation of dormant *Bacillus subtilis* spores. *J. Bacteriol.* **198**, 168–177 (2016).
45. Ghosh, S. et al. Characterization of spores of *Bacillus subtilis* that lack most coat layers. *J. Bacteriol.* **190**, 6741–6748 (2008).
46. Nagler, K. et al. Involvement of coat proteins in *Bacillus subtilis* spore germination in high-salinity environments. *Appl. Environ. Microbiol.* **81**, 6725–6735 (2015).
47. Wells-Bennik, M. H. J. et al. Bacterial spores in food: survival, emergence, and outgrowth. *Annu. Rev. Food Sci. Technol.* **7**, 457–482 (2016).
48. Driks, A., Roels, S., Beall, B., Moran, C. P. & Losick, R. Subcellular localization of proteins involved in the assembly of the spore coat of *Bacillus subtilis*. *Genes Dev.* **8**, 234–244 (1994).
49. McKenney, P. T., Driks, A. & Eichenberger, P. The *Bacillus subtilis* endospore: assembly and functions of the multilayered coat. *Nat. Rev. Microbiol.* **11**, 33–44 (2013).
50. Yoon, J., Cai, S., Suo, Z. & Hayward, R. C. Porelastic swelling kinetics of thin hydrogel layers: comparison of theory and experiment. *Soft Matter* **6**, 6004–6012 (2010).
51. Raviv, L., Laurat, P. & Klein, J. Fluidity of water confined to subnanometre films. *Nature* **413**, 51–54 (2001).
52. Patil, S., Matei, G., Oral, A. & Hoffmann, P. M. Solid or liquid? solidification of a nanoco confined liquid under nonequilibrium conditions. *Langmuir* **22**, 6485–6488 (2006).
53. Pearce, S. P. et al. Finite indentation of highly curved elastic shells. *Proc. R. Soc. A* **474**, 20170482 (2018).
54. Popov, V. L., Heß, M. & Willert, E. *Handbook of Contact Mechanics: Exact Solutions of Axisymmetric Contact Problems* (Springer Nature, 2019).
55. Puttock, M. & Thwaite, E. *Elastic Compression of Spheres and Cylinders at Point and Line Contact* (Commonwealth Scientific and Industrial Research Organization, 1969).
56. Garcia, P. D. & Garcia, R. Determination of the elastic moduli of a single cell cultured on a rigid support by force microscopy. *Biophys. J.* **114**, 2923–2932 (2018).
57. Fletcher, N. H. In *The Chemical Physics of Ice* 165–197 (Cambridge Univ. Press, 1970).
58. Harrelson, S. G. et al. Data for hydration solids. *figshare* <https://doi.org/10.6084/m9.figshare.22189823> (2023).
59. Plomp, M., Leighton, T. J., Wheeler, K. E. & Malkin, A. J. The high-resolution architecture and structural dynamics of *Bacillus* spores. *Biophys. J.* **88**, 603–608 (2005).
60. Pasquina-Lemonche, L. et al. The architecture of the Gram-positive bacterial cell wall. *Nature* **582**, 294–297 (2020).
61. Setlow, P. Spores of *Bacillus subtilis*: their resistance to and killing by radiation, heat and chemicals. *J. Appl. Microbiol.* **101**, 514–525 (2006).
62. Dittmann, C., Han, H.-M., Grabenbauer, M. & Laue, M. Dormant *Bacillus* spores protect their DNA in crystalline nucleoids against environmental stress. *J. Struct. Biol.* **191**, 156–164 (2015).
63. Lee, S. A. et al. A Brillouin scattering study of the hydration of Li- and Na-DNA films. *Biopolymers* **26**, 1637–1665 (1987).
64. Cowan, A. E., Koppel, D. E., Setlow, B. & Setlow, P. A soluble protein is immobile in dormant spores of *Bacillus subtilis* but is mobile in germinated spores: implications for spore dormancy. *Proc. Natl. Acad. Sci. USA* **100**, 4209–4214 (2003).
65. Sunde, E. P., Setlow, P., Hederstedt, L. & Halle, B. The physical state of water in bacterial spores. *Proc. Natl. Acad. Sci. USA* **106**, 19334–19339 (2009).

# Article

**Acknowledgements** We acknowledge A. Driks (Department of Microbiology and Immunology, Loyola University Chicago, Maywood, IL, USA) who passed away before the completion of the work for contributing spores, and for discussions that informed the hygroelastic theory and for suggesting the use of known sieving properties of spores as an estimate of pore size. Funding was provided by US Department of Energy (DOE) Early Career Research Program, Office of Science, Basic Energy Sciences (BES), under award no. DE-SC0007999 (Fig. 1 and experimental data in Figs. 3 and 4); by the Office of Naval Research, under award nos. N00014-19-1-2200 (Fig. 5 and theoretical analyses in Figs. 3 and 4) and N00014-21-1-4004 (theoretical analyses in Figs. 3 and 4); by the National Institute of General Medical Sciences of the National Institutes of Health, under award nos. R35GM141953 (to J.D.) and R35GM145382 (to O.S.); and by the David and Lucile Packard Fellows Program. We acknowledge the use of facilities and instrumentation supported by NSF through the Columbia University, Columbia Nano Initiative, and the Materials Research Science and Engineering Center DMR-2011738.

**Author contributions** M.D., X.C. and O.S. designed the experiments probing relaxation kinetics with nanomechanical cantilever sensors. M.D. and X.C. developed the experimental apparatus for relaxation kinetics measurements. M.D. conducted the relaxation kinetics measurements. M.D., S.G.H., A.-H.C. and O.S. contributed to the analysis of relaxation kinetics measurements. M.D. and S.G.H. conducted spore height measurements. X.C. conducted force-distance curve

measurements. S.G.H. and O.S. analysed measurements of water-responsive size change and nonlinear elasticity of spores. S.G.H. and O.S. designed experiments probing the hygroelastic transition. S.G.H. conducted the experiments probing the hygroelastic transition and analysed the data. H.A.S. contributed to the theoretical analysis of the hygroelastic transition. J.D. contributed materials. O.S. conceived the hygroelastic model. S.G.H. aided in the development and refinement of the hygroelastic model. M.D., S.G.H., J.D., H.A.S. and O.S. contributed to the discussions. O.S. designed the research. M.D., S.G.H. and O.S. prepared the paper with input from all authors.

**Competing interests** The authors declare no competing interests.

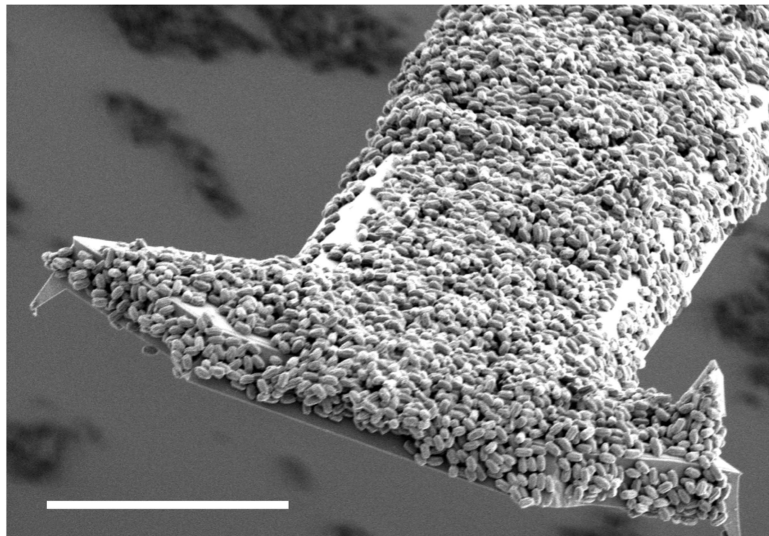
## Additional information

**Supplementary information** The online version contains supplementary material available at <https://doi.org/10.1038/s41586-023-06144-y>.

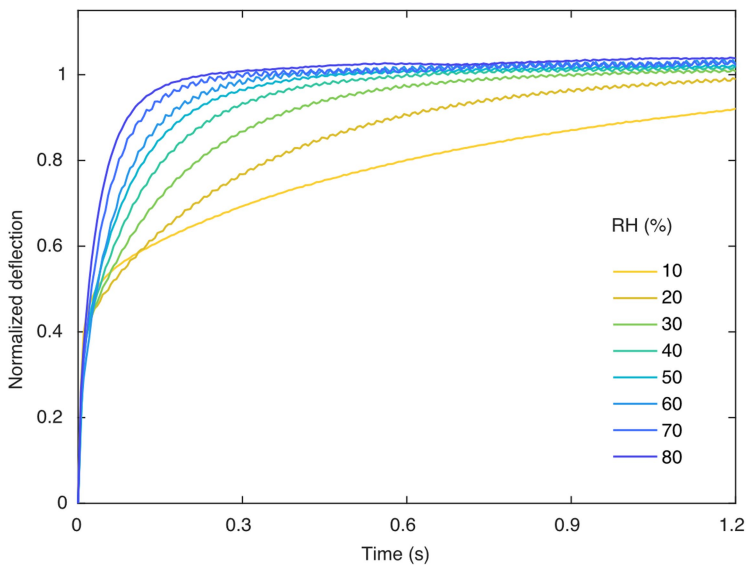
**Correspondence and requests for materials** should be addressed to Ozgur Sahin.

**Peer review information** *Nature* thanks Peter Hoffmann and the other, anonymous, reviewer(s) for their contribution to the peer review of this work. Peer reviewer reports are available.

**Reprints and permissions information** is available at <http://www.nature.com/reprints>.

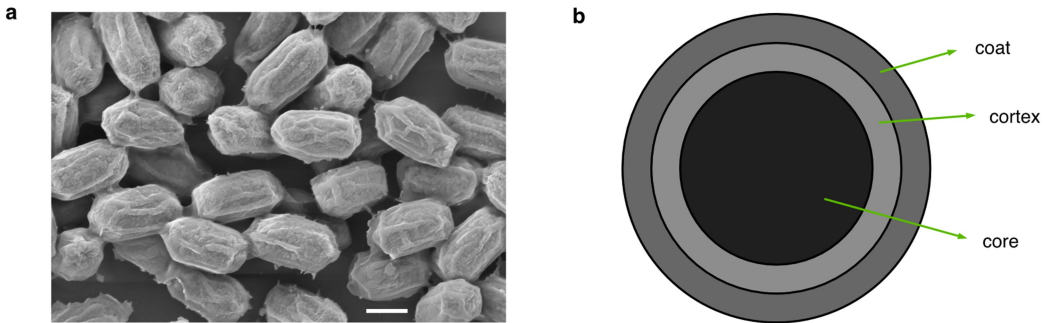


**Extended Data Fig. 1 | Spore-coated cantilever.** Scanning electron microscopy image of a spore-coated cantilever. Scale bar -20  $\mu\text{m}$ . The cantilever is T-shaped, and it is approximately 300  $\mu\text{m}$  long and 30  $\mu\text{m}$  wide, except near the free end where the width is approximately 60  $\mu\text{m}$ .



**Extended Data Fig. 2 | Cantilever deflection signals.** Representative cantilever deflection signals following photothermal pulses shown for a range of relative humidity levels. Deflection signals are normalized so that

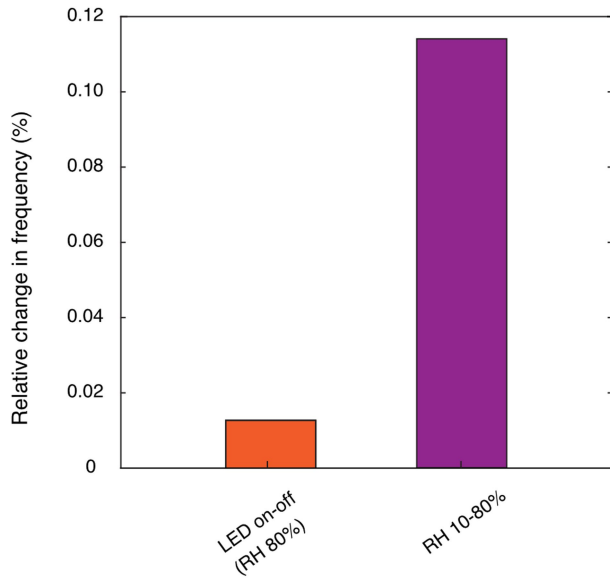
peak-to-peak deflection corresponds to 1. All curves are obtained with the same spore-coated cantilever. They are representative of curves from all five cantilevers used in Fig. 1d.



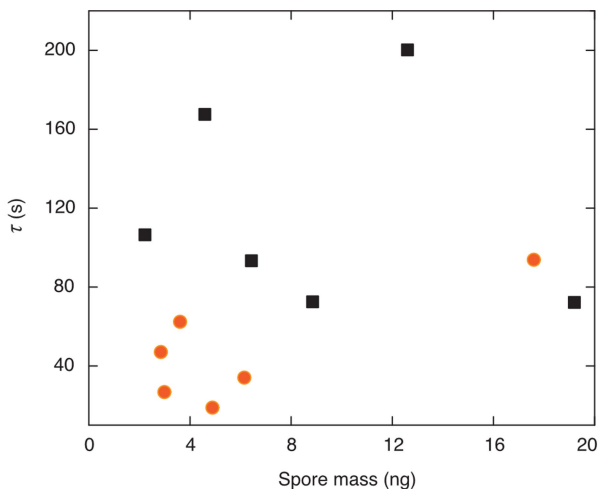
**Extended Data Fig. 3 | Microstructure and properties of spores.** a, Scanning electron microscopy image of the spores of *B. subtilis*. Scale bar: 500 nm. Wild type spores of *B. subtilis* are approximately 650 nm in diameter and 1  $\mu$ m to 1.5  $\mu$ m in length. b, Illustration of the cross section of spores of *B. subtilis* showing the cortex and coat layers that surround the core, which contains the genetic material. The coat is a proteinaceous, water-permeable layer<sup>49</sup>. AFM images of the outer surface of the coat reveal an assembly of parallel rodlets formed by coat proteins with ~8 nm periodicity<sup>50</sup>. The cortex, also a water permeable layer, is a loosely crosslinked network of peptidoglycan that is similar in structure to that of vegetative cells. The vegetative peptidoglycan in *B. subtilis* has an average diameter of 4 nm, as observed in AFM images<sup>60</sup>.

The thicknesses of the coat and the cortex layers are approximately 70 nm each (see Methods). The spore core contains proteins and DNA. The core is dehydrated<sup>61</sup> and the DNA is packed in a crystalline state<sup>62</sup>. Elastic modulus measurements of DNA films in crystalline state show the Young's modulus of these films to be approximately 1.1 GPa<sup>63</sup>, suggesting that the core is a stiff solid rather than a fluid. This assumption is also supported by the observation that soluble biomolecules are immobile in the dehydrated cores of dormant spores but gain mobility upon germination when the core gets hydrated<sup>64</sup>. The spore water, however, exhibits rotational mobility, as indicated by the observations of short rotational correlation times of D<sub>2</sub>O in spores<sup>65</sup>. This observation also indicates that water in spores is not in an ice-like (solid) state.

## Article



**Extended Data Fig. 4 | Relative effect of the photothermal pulse.** Shifts in the resonance frequency of spore-coated cantilevers are sensitive to the amount of water exchange. We used this effect to compare relative effects of the photothermal pulse and RH. Here we plot the relative changes in fundamental resonance frequency of a cantilever coated with spores in two cases: (left, red bar) as a result of photothermal pulse and (right, purple bar) in response to a change in relative humidity from 80% to 10%. The results are given as percentages. They indicate that the perturbation due to the photothermal pulse is small, and therefore, the transient deflections of the cantilever in response to photothermal pulses reflect approximately the state of the spore at the set-point level of the relative humidity.



**Extended Data Fig. 5 | Time constants and the total spore mass.** The spore quantities are represented by spore mass estimated from the shifts in cantilever resonance frequencies. Time constants are plotted for wild type *B. subtilis* (square) and *B. subtilis cotEgerE* (circle) spores. According to the data, there is a lack of clear association between the time constant and the total spore mass, however the effect of spore type results in a statistically significant change in time constants: Mean time constant at 50% RH for wild type *B. subtilis* [square] is -118 ms and -47.1 ms for *B. subtilis cotEgerE* [circle] (one-tailed T, p < .01).